A COMPLEX ENVIRONMENT AROUND CIRCINUS X-1

A. D'Aí,[1] R. Iaria,[1] T. Di Salvo,[1] G. Lavagetto,[1] and N. R. Robba[1]

ABSTRACT

We present the results of an archival 54 ks long *Chandra* observation of the peculiar source Cir X-1 during the phase passage 0.223-0.261. We focus on the study of detected emission and absorption features using the HETGS. A comparative analysis of X-ray spectra, selected at different flux levels of the source, allows us to distinguish between a very hard state, at a low count rate, and a brighter, softer, highly absorbed spectrum during episodes of flaring activity. The spectrum of the hard state clearly shows emission lines of highly ionized elements, while, during the flaring state, the spectrum also shows strong resonant absorption lines. The most intense and interesting feature in this latter state is present in the Fe Kα region: a very broadened absorption line at energies $\sim$6.5 keV that could result from a smeared blending of resonant absorption lines of moderately ionized iron ions (Fe xx–Fe xxiv). We also observe strong resonant absorption lines of Fe xxv and Fe xxvi, together with a smeared absorption edge above 7 keV. We argue that the emitting region during the quiescent/hard state is constituted of a purely photoionized medium, possibly present above an accretion disk, or of a photoionized plasma present in a beamed outflow. During the flaring states the source undergoes enhanced turbulent accretion that modifies both the accretion geometry and the optical depth of the gas surrounding the primary X-ray source.

Subject headings: line: formation — line: identification — stars: individual (Circinus X-1) — X-rays: binaries — X-rays: general

1. INTRODUCTION

Cir X-1 is a peculiar low-mass X-ray binary (LMXB), probably hosting a neutron star (NS), because of the presence of type-I X-ray bursts detected during an *EXOSAT* observation (Tennant et al. 1986). The first long-term X-ray light curve showed a periodicity of $\sim$16.6 days (Kaluzienski et al. 1976) that was interpreted as an effect of an orbital period. This modulation is also observed in the radio band (Haynes et al. 1978) and in the IR (Glass 1994; Clark et al. 2003).

Based on the presence of a nearby ($\sim$25′) supernova remnant, SNR G321.9−0.3, Clark et al. (1975) first hypothesized that Cir X-1 could be a runaway binary system, expelled from the site of the supernova explosion with a high-velocity kick. The hypothesis gained significant attention, also thanks to resolved radio maps that showed Cir X-1 is embedded inside a radio nebula (Haynes et al. 1986) with jets (Fender et al. 1998), bending toward the position of the SNR.

These jets have ultrarelativistic velocities (Fender et al. 2004), similar to those produced by active galactic nuclei and galactic microquasars, thus ruling out the belief that only black holes are able to launch relativistic outflows. The angle between our line of sight and the direction of the jet was inferred to be less than 5°. More recently the jets have also been resolved in the X-ray (Heinz et al. 2007).

The connection between SNR G321.9−0.3 and Cir X-1 seems, however, now to be compromised by some *Hubble Space Telescope* observations (Mignani et al. 2002) that showed no apparent proper motion (with an upper limit of 200 km s^{-1}), contrary to what had been expected (Tauris et al. 1999).

The 16.6 cycle, although first detected in the X-ray, has been largely studied in the radio wavelength. Based on the onset times of radio flares observed between 1978 and 1988, Stewart et al.

(1991) derived the ephemeris of the source, giving, for phase 0, the following formula:

$$\mathrm{MJD}_N = 43076.37 + N(16.5768 - 3.53 \times 10^{-5}N), \quad (1)$$

which constituted, for more than a decade, the reference ephemeris for the source. Recently, Parkinson et al. (2003) using only X-ray data spanning a period of 30 yr, obtained the first X-ray ephemeris. However, the analysis was based on the occurrence of periods of X-ray maxima in the X-ray light curves, which Clarkson et al. (2004) argued could be flawed by large intrinsic phase scattering, thus leading to systematic errors. Adoption of the periastron X-ray dips was found to provide, therefore, a more suitable system clock, thus resulting in the new ephemeris

$$\mathrm{MJD}_N = 50081.76 + N(16.5732 - 2.15 \times 10^{-4}N). \quad (2)$$

This solution implies, moreover, a significant high orbital period derivative, resulting in a characteristic life timescale, $P/2\dot{P}$, for the system of $\sim$1000 yr. Clarkson et al. (2004) concludes that Cir X-1 is, indeed, a very young system, whose SNR could be the same radio nebula in which it is embedded. Tudose et al. (2006) derived, under the assumption that the radio nebula is, instead, powered by jet activity, a nebula lifetime in the 4×10^3 to 4×10^5 yr range and a jet injected power of $\sim 10^{35}$ ergs s^{-1}.

The companion star in Cir X-1 has been long searched for, but the high visual extinction toward the direction of the source has prevented its determination. Recently, Jonker et al. (2007), through optical *I*-band monitoring of the emission/absorption Paschen lines seen in the optical spectra of the system and assuming that the lines are produced by the companion star, have derived the best-fitting orbital parameters of the system: an eccentricity $e = 0.45$, orbital period = 16.6 days, and a sin i = 16.9 lt-s. The companion star is, assuming a mass for the compact object of 1.4 $M_\odot$, a supergiant of B5−A0 stellar type, whose mass should be $\leq$10 $M_\odot$, while the inclination of the system should be $\geq$14°.

[1] Dipartimento di Scienze Fisiche ed Astronomiche, Università di Palermo, via Archirafi 36-90123, Palermo, Italy; dai@fisica.unipa.it.

This X-ray source shows some spectral behaviors similar to those shown by black hole (BH) binaries, but others that are most similar to those shown by NS binaries, making the nature of this system quite enigmatic. The X-ray spectrum of Cir X-1 has been extensively studied in the past for each phase of the orbital period. The continuum emission consists of a thick Comptonized component (Iaria et al. 2001b), which, for relatively narrow band coverage, cannot be distinguished from a simpler sum of two thermal components, and a variable hard tail above 10 keV (Iaria et al. 2001a). The spectrum shows a phase-dependent evolution, whose major characteristic, when the source is near the periastron passage, is the appearance of a large column density of neutral matter occulting the continuum X-ray emission. Its origin has been assigned or in the colder outer layers of the accretion disk, or alternatively in the occulting presence of the companion star (Brandt et al. 1996). The first interpretation, however, implies an edge-on geometry, which is in contrast with the observed small angle of view of the jet.

High-resolution spectra obtained with *Chandra* (Schulz & Brandt 2002, hereafter Paper I) showed P Cygni profiles of H- and He-like ions, whose intensity decreased with decreasing luminosity of the source. The P Cygni structures were all blueshifted with respect to the expected laboratory-frame energies, thus leading to the conclusion that these features could arise from a radiatively or thermally driven wind from a hard X-ray irradiated accretion disk. The spectrum also shows complex absorption features above 7 keV, whose intensity and position vary according to the orbital phase (Iaria et al. 2001b).

Timing properties have also been also extensively studied in the past, but recently Boutloukos et al. (2006) have shown, using a large sample of archival *RXTE* data, that the timing behavior is very similar to the one displayed by the bright accreting NS systems, belonging to the class of the Z sources. The mostly notable characteristic is the presence of twin kilohertz quasi-periodic oscillations (kHz QPOs) in the power spectrum of the source at peak frequencies in the 56−223 Hz range for the lower peak and 230−550 Hz for the upper peak. However, the frequency range of the kHz QPOs in Cir X-1 is significantly lower than the one shown by other accreting NS sources (see also Belloni et al. 2007).

Cir X-1 seems, therefore, to share the basic ingredients of the class of the old, low-magnetized, bright NS systems, although the high inferred eccentricity, the variable phase-dependent spectral changes, and the very probable young age do not fit into the classical Z classification scheme. Observations of spectral and timing features common to physical objects of such different physical characteristic, therefore, offer a unique opportunity to test present theories against experimental data.

In this work we present a detailed spectral analysis of Cir X-1 using a 54 ks long *Chandra* observation. We analyzed the source when it was highly variable, but only within a restricted orbital phase. This allowed us to investigate how the emission and absorption lines change with the continuum without having to consider the complicating effects of the change in phase. Through X-ray spectra of this source selected at different flux levels, we show the complex spectral changing of the source; data clearly indicate that the emission-line features are present both during the quiescent state and the flaring state of the source, while it is only during the flaring activity, when the source count rate strongly rises, that the spectrum shows strong absorption features of highly ionized iron and calcium. The appearance of these features is linked to the continuum emission, which strongly varies, becoming, from the quiescent to the flaring states, more luminous, but at the same time, completely obscured by a large column density of cold material.

2. OBSERVATION AND DATA REDUCTION

Cir X-1 was observed with the *Chandra* observatory on 2005 June 2 from 08:35:58 to 23:44:51 UT using the High Energy Transmission Grating Spectrometer (HETGS), for a total integration time of 52650 s (Obs ID. 5478, from the *Chandra* public archive). The corresponding orbital phase, using the ephemeris of Stewart et al. (1993), lies between 0.065 and 0.104, based on the phase-zero passage at the periastron. Adopting the ephemeris of Clarkson et al. (2004), this corresponds to the phase range 0.223−0.261. The observation was performed in timed faint mode, adopting a subarray (512 rows) of the ACIS-S detector to mitigate the effects of photon pile-up, with a CCD frame time of 1.7 s. We processed the event list using available software (FTOOLS ver. 6.1.2 and CIAO ver. 3.2 packages). We computed aspect-corrected exposure maps for each spectrum, allowing us to correct for effects from the effective area of the CCD spectrometer. The brightness of the source prevented the study of the zeroth-order events since these are mostly affected by pile-up. On the other hand, the grating spectra are not, or are only moderately (less than 10%), affected. In this work we utilize the first-order HEG and MEG spectra. Data were extracted from regions around the grating arms; to avoid overlapping between HEG and MEG data, we used a region size of 25 and 33 pixels for the HEG and MEG, respectively, along the cross-dispersion direction. The background spectra were computed, as usual, by extracting data above and below the dispersed flux. We used the standard CIAO tools to create detector response files for the HEG−1 (MEG−1) and HEG+1 (MEG+1) order (background-subtracted) spectra. To compute as accurately as possible the position of the zeroth order, we extracted the event list during a time interval when the source showed the lowest count rate and variability; from the zeroth-order image we derived the counts pixel^{-1} grid. The center of the pixel showing the highest counting corresponds to the FK5 (J2000.0) coordinates R.A. = $15^h20^m40.87^s$ and decl. = $-57°10'00.24''$, with an error on the coordinates of $0.6''$. The identification of the zeroth order is in agreement with the result of Iaria (2007) when the source during another *Chandra* observation was in a very low luminosity state and the zeroth order was not affected by pile-up issues. After verifying that the negative and positive orders were compatible with each other in the whole energy range, we co-added them using the script add_grating_spectra in the CIAO software, obtaining the first-order MEG spectrum and the first-order HEG spectrum. HEG and MEG spectra were finally rebinned in order to have at least 25 counts per energy channel to allow the use of χ^2 statistics. We used MEG and HEG spectra in the 1.3−5.0 and the 1.5−9.0 keV energy ranges, respectively. In Figure 1 we show the 256 s bin-time light curve taking into account only the events in the first-order HEG and MEG diffracting regions in two energy bands. The topr panel shows the temporal behavior of the low-energy photons (1.0−4.0 keV), while center panel shows the same in the high-energy band (4.0−9.0 keV). The two light curves follow the same pattern of variability, with a low count rate at the beginning of the observation, lasting less than 20 ks, with three short-term peaks; the second part of the observation is characterized by intense source variability with three broad peak profiles where the count rate rises by more than an order of magnitude in both bands. In the bottom panel of the curve we show the hardness ratio of the two energy bands, which is slightly anticorrelated with respect to the count rates (see also Shirey et al. 1999 for a discussion on the spectral hardening evolution of the source).

The light curve for the whole energy band, for the same extracting regions, has an average count rate of ~ 0.47 counts s^{-1}
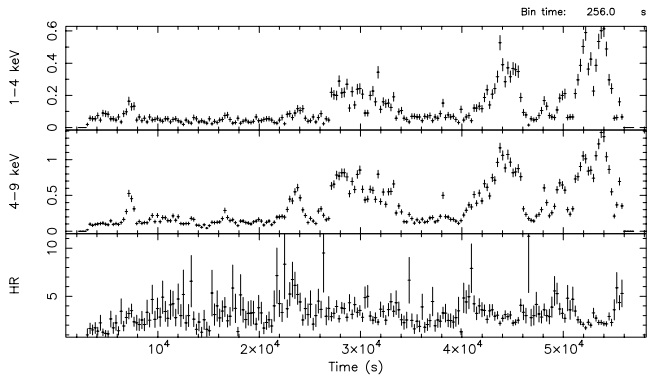
FIG. 1.—Light curves of Cir X-1 *Chandra* observation. *Top:* A 1.0–4.0 keV light curve of Cir X-1 *Chandra* observation extracted from selected regions around the HEG and MEG first-order arms. *Center:* 4.0–9.0 keV light curve using the same regions of top panel. *Bottom:* Hardness ratio of the energy bands [4.0–9.0]/[1.0–4.0].
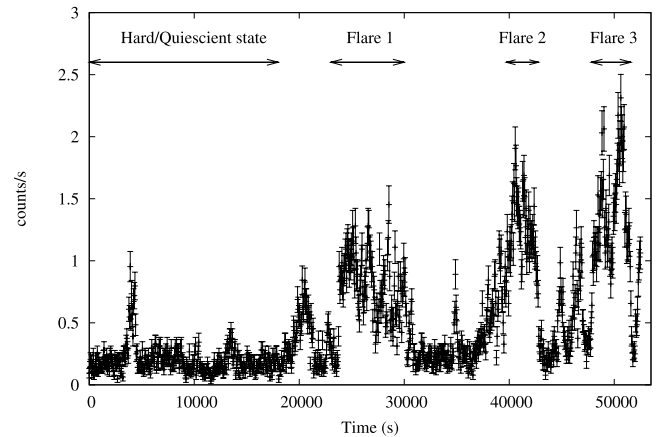

FIG. 2.—Light curve of Cir X-1 *Chandra* observation extracted from selected regions around the HEG and MEG first-order arms. Above the light curve, arrows delimit the time intervals that we used to extract the time-selected spectra. The bin time in the light curve is set to 64 s.

and it is shown in Figure 2. Given the strong variability of the source we performed a time-selected spectral analysis based on the count rate variability of the source. The first time-selected state lies in the first part of the observation, when the source shows the lowest count rate and presents the minimum level of variability. From this time selection we, however, excluded two short minor peaks present in the light curve. The total collecting time for this state is ~17.3 ks, with an average count rate of 0.35 counts s^{-1}. The second time-selected spectrum encompasses the peak of the first broad flare, for a time duration of 7.3 ks with an average count rate of 1.38 counts s^{-1}. The third state is centered around the second, sharper, peak, while the fourth state is centered in the last segment of the observation. The collecting time and the average count rate for these selections are 3.10 ks and 1.15 counts s^{-1}, and 3.84 ks and 1.32 counts s^{-1}, respectively. We show in Figure 2 the light curves of the entire observation and of the time-selected intervals.

We considered negligible the level of pile-up for our observation. We left a normalization constant between the HEG and MEG spectrum free to vary, in order to take into account residual flux calibration uncertainties. For the spectral analysis we used the software package XSPEC 11.3.2p.

3. SPECTRAL ANALYSIS

3.1. *The Time-selected Spectra: The Quiescent State*

In order to fit to the continuum emission of the source we adopted a spectral decomposition that closely follows previous models (e.g., Brandt et al. 1996; Iaria et al. 2001b; Schulz & Brandt 2002): an absorbed thermal component (bbody in XSPEC) multiplied by a partial covering component (pcfabs in XSPEC), while the value of the interstellar absorption (wabs in XSPEC) was frozen to a reference value of 1.85×10^{22} cm^{-2} adopting the cross sections from Morrison & McCammon (1983). The partial covering component is strictly required by the fit; a simpler wabs*bb model gives an unrealistically high value for the blackbody temperature ($kT_{bb} \geq 9$ keV) and a corresponding high value for the interstellar equivalent hydrogen column. The blackbody temperature is ~3 keV, with a corresponding blackbody radius of 0.5 ± 0.1 km. The model is insensitive to the addition of further spectral components. The blackbody component can be replaced by a flat power law (photon index $= -0.1^{+0.4}_{-0.5}$) without significant change in the χ^2 value of the fit and in the other spectral parameters. The continuum flux is significantly obscured by the partial covering effect, with an associated equivalent hydrogen column

$N_H = 16^{+5}_{-3} \times 10^{22}$ cm^{-2} and a covering fraction $f = 0.69^{+0.07}_{-0.06}$. The shape of the spectrum is quite peculiar, and, as far as we know from literature, this is the hardest spectrum ever observed in this source. The absorbed flux in the *Chandra* energy range (1.0–10 keV) corresponds to 1.56×10^{-10} ergs cm^{-2} s^{-1}, while extrapolating in a wider range (0.01–100 keV) results in a flux of 4.63×10^{-10} ergs cm^{-2} s^{-1}. We note, however, that this simplified continuum model, although it clearly indicates a rather hard spectrum, is not suited for the study of the continuum behavior of the source, given the restricted energy band of *Chandra*, and a more complex spectral decomposition is expected for this kind of source. In fact, the continuum emission, which we fitted with a single-temperature blackbody, does not reproduce a typical accreting NS spectrum, which has softer thermal temperatures and generally presents two or more temperature peaks. The following analysis, therefore, mainly focuses on the detection of narrow discrete absorption/emission features. We tested for their presence by adopting different continuum models (such as the best-fitting model discussed above, polynomial fits in a narrow band around the features, power-law fits), and although we observed slight changes in their detection thresholds or parameter space, we found that the overall picture and the conclusions derived are not affected by the particular continuum that was adopted. We caution the reader, however, that a significant discrepancy, dependent on the model adopted, can arise for the determination of the optical depth of iron edges above 7 keV, as the continuum cannot be sufficiently well constrained above these energies. The spectrum is characterized by some clear discrete features; adopting our best-fit continuum, we detect, with a significance always above 3 σ, three emission lines at energies consistent with resonant emission lines of H-like Si, He-like Ca, and He-like Fe, a rather narrow absorption line at 6.49 ± 0.03 keV, and a 6.4 keV emission line, possibly associated with fluorescence emission from neutral, or lowly ionized, iron. Above 7 keV we found a strong absorption edge at energies correspondent to the neutral Fe Kα edge. The emission lines from highly ionized elements are narrow, as we find only upper values to the line widths (7, 25, and 28 eV for Si xv, Ca xix and Fe xxv, respectively). The detection of the iron fluorescence line at energies ~6.4 keV indicates the presence of a cold reflecting medium, which is also responsible for the sharp edge observed at higher energies. From the optical depth of the edge ($\tau = 1.2^{+0.3}_{-0.4}$), we infer that the associated equivalent hydrogen column is $(6 \pm 2) \times 10^{24}$ cm^{-2}, a very high value that exceeds by an order of magnitude the value reported by

TABLE 1
THE CONTINUUM EMISSION

Parameter	Hard State	Flaring State	Integrated
kT_{bb} (keV)	$3.07^{+0.7}_{-0.1}$	1.68 ± 0.03	$2.19^{+0.15}_{-0.11}$
L_{bb} (10^{36} ergs s^{-1})	2.88 ± 0.07	7.5 ± 0.2	4.68 ± 0.36
pcfabs N_H (10^{22})......	16^{+5}_{-3}	9.2 ± 0.3	$9.0^{+0.5}_{-0.7}$
pcfabs cvr frac......	$0.69^{+0.07}_{-0.06}$	0.974 ± 0.005	0.93 ± 0.01
smedgeE (keV)	$7.16^{+0.07}_{-0.03}$	$7.13^{+0.13}_{-0.06}$	$7.0^{+0.04}_{-0.11}$
smedge τ...................	$1.2^{+0.3}_{-0.4}$	$0.9^{+0.1}_{-0.2}$	$1.24^{+1.0}_{-0.25}$
smedge width.............	$0^{+0.2}$	$0.42^{+0.4}_{-0.15}$	$0.54^{+0.8}_{-0.18}$
χ^2/dof.......................	160/316	749/1078	1004/1384

NOTES.—Fitting results for the continuum model in the Cir X-1 HEG/MEG co-added spectra. Data have been rebinned up that a minimum of 25 counts channel^{-1}. Uncertainties are reported at 90% confidence level for a single parameter; upper limits at 95% confidence level.

Shirey et al. (1999) when the source was in a dip state. We also tested the possibility that this edge could be partially smeared using the smedge component in XSPEC (Ebisawa 1991), keeping fixed the index for the photoelectric cross section at the default value of -2.67. We did not find, in this case, any evidence of smearing, with only an upper value of the smearing width of 0.2 keV. We report in Table 1 the values and the uncertainties for

the best-fitting parameters for the continuum emission, while in Table 2 we report the corresponding parameters for the detected lines. Errors are always reported at $\Delta\chi^2 = 2.7$. We show in the left panels of Figures 3, 4, and 5 the plot of data, with the best-fit model in the energy ranges 1.4–2.7, 3.8–4.2, and 6.2–7.4 keV superimposed.

3.2. *The Time-selected Spectra: The Flaring States*

During this *Chandra* observation we observe the source undergoing episodes of flaring activity; we distinguish three long flares, of approximately 8, 5.4, and 4 ks duration, and seven short minor flares. We time selected three energy spectra, extracted from the light curve, centered at the count rate peaks of the long flares and performed a spectral analysis using the same data reduction criteria of the quiescent state extraction. We will simply refer to these spectra as the flare 1, 2, or 3 spectrum for the first, second, and the third long flares present in the light curve, respectively (see Fig. 2). For the continuum emission of the source we adopted the same model of the quiescent state, with the same spectral parameters free to vary.

The spectra show in all the flaring states a significant change both in the primary continuum emission and in the absorbing medium with respect to the hard state. The blackbody temperature drops to ~1.6 keV from the ~3 keV temperature of the

TABLE 2
CIR X-1 EMISSION AND ABSORPTION LINES

Ion	Measured E (keV)	Predicted E[a] (keV)	Width (eV)	Equivalent Width (eV)	Flux ($\times 10^{-4}$) (photons cm^{-2} s^{-1})
			Hard State		
Si XIV	2.0046 ± 0.0019	2.0054	3^{+4}_{-3}	57^{+43}_{-36}	$1.8^{+0.9}_{-0.8}$
Ca XIX.................................	$3.889^{+0.013}_{-0.009}$	3.902	8^{+17}_{-8}	17^{+10}_{-11}	$0.7^{+0.5}_{-0.6}$
Fe I	6.403 ± 0.016	6.400	24^{+22}_{-14}	26 ± 20	1.1 ± 0.5
Fe blended..........................	6.49 ± 0.03	...	50^{+40}_{-30}	-30^{+20}_{-37}	$-2.0^{+0.9}_{-1.3}$
Fe XXV	$6.679^{+0.011}_{-0.015}$	6.700	11^{+16}_{-11}	-33 ± 25	1.4 ± 0.6
			Flaring State (sum)		
Si XIV	2.0043	2.0054	2^{+6}_{-2}	35 ± 10	14^{+13}_{-8}
S XVI	2.6181	2.6216	4.2	7^{+10}_{-7}	3^{+4}_{-3}
Ca XIX.................................	$3.911^{+0.005}_{-0.017}$	3.902	3^{+12}_{-3}	-7^{+4}_{-50}	$-2^{+0.8}_{-17}$
Ca XX.................................	4.1065 ± 0.0025	4.1049	3^{+4}_{-3}	-10^{+3}_{-2}	-3.0 ± 0.9
Fe I	6.398	6.400	16	15 ± 13	2.4 ± 2.0
Fe blended..........................	6.568 ± 0.020	...	84^{+17}_{-22}	-125^{+35}_{-25}	-23 ± 5
Fe XXV	$6.701^{+0.013}_{-0.010}$	6.700	11^{+33}_{-11}	-23^{+18}_{-15}	$-3.2^{+1.8}_{-5}$
Fe XXVI	$6.972^{+0.013}_{-0.009}$	6.966	13^{+18}_{-13}	-36^{+13}_{-10}	$-5.5^{+1.9}_{-2.6}$
			Integrated Spectrum		
Mg XII (Lyα).....................	$1.4717^{+0.0025}_{-0.0021}$	1.4723	2	40 ± 20	4.3 ± 2.2
Mg XII (Lyβ)	1.748 ± 0.003	1.745	2	18 ± 10	$2.1^{+8.0}_{-1.9}$
Mg XII (Lyγ)[b]	1.8395 ± 0.0015	1.8400	$5.3^{+1.5}_{-2.0}$	19^{+5}_{-9}	$2.4^{+0.6}_{-1.1}$
Si XIV	2.0043 ± 0.0011	2.0054	3.5 ± 1.1	64^{+7}_{-12}	$8.1^{+1.9}_{-1.7}$
S XV f	2.4307	2.4307	2	10^{+6}_{-8}	$1.3^{+1.9}_{-1.7}$
S XVI	2.618 ± 0.003	2.6216	4.2 ± 3.1	22 ± 9	$3.1^{+1.3}_{-1.1}$
Fe I	6.398 ± 0.009	6.400	16^{+11}_{-16}	26^{+20}_{-12}	$2.3^{+1.7}_{-1.0}$
Ca XIX f	3.8612	3.8612	2	$3.2^{+2.0}_{-1.7}$	0.4 ± 0.3
Ca XX.................................	4.109 ± 0.003	4.105	$1.1^{+4.0}_{-1.1}$	-6.0 ± 1.8	-0.82 ± 0.23
Fe blended..........................	6.541 ± 0.015	...	95 ± 20	-125^{+24}_{-20}	$-13.1^{+2.4}_{-2.6}$
Fe XXV	6.713 ± 0.012	6.7002	18 ± 15	-20 ± 10	$-1.6^{+0.8}_{-0.9}$
Fe XXVI	6.979 ± 0.008	6.966	25 ± 12	-38 ± 10	-2.3 ± 1.0

NOTES.—Fitting results from emission and absorption lines in the Cir X-1 HEG and MEG spectra. Uncertainties are reported at 90% confidence level for a single parameter; upper limits at 95% confidence level.

[a] The predicted values of the detected line energies are reported by Verner et al. (1996).

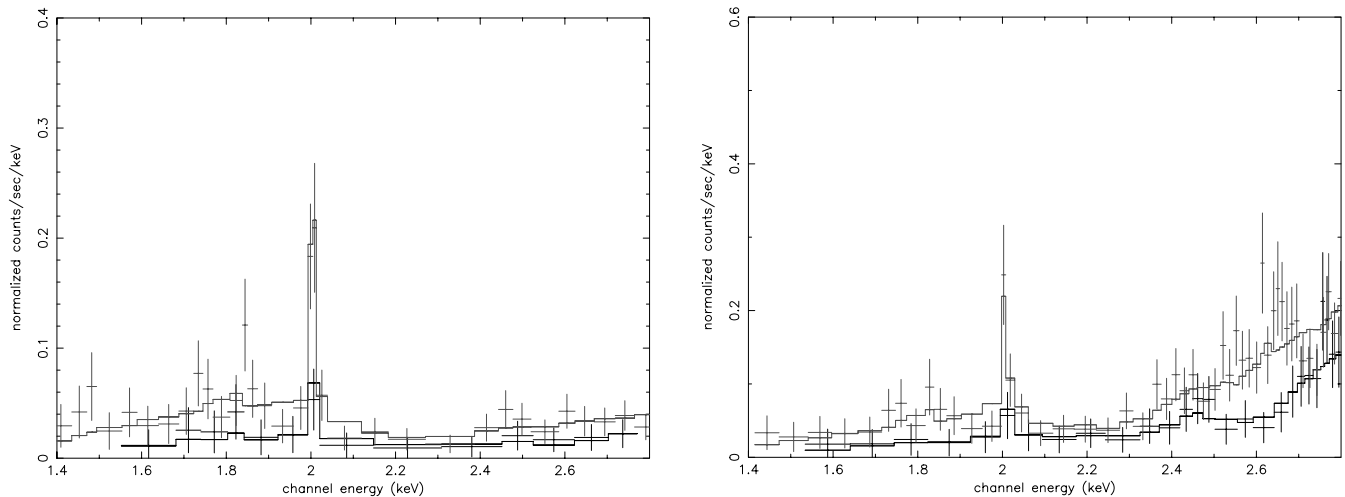[b] The line is very probably blended with the forbidden line of Si XIII.

Fig. 3.—*Left:* Data together with best-fit model in the low-energy band (1.4−2.7 keV) during the hard/quiescent state. *Right:* The same region in the total flare time integrated spectrum. The only feature clearly seen in both spectra is the Lyα emission line of Si XIV at ∼2 keV. MEG data are shown in red, HEG data in black.

quiescent state, while the unabsorbed luminosity results more than doubled (see Table 3). We note, however, that a power-law component could replace the blackbody component without significantly changing the χ^2 value of the fit. In this case we found for all the flaring spectra value of the power-law index in the 1.5−2.2 range. The partial covering matter during the first flare has the same equivalent hydrogen column as during the quiescent state, while the covering fraction of the obscuring medium covers up to ∼94% of the total continuum emitting region. During the second and the third flare, the continuum flux continues to rise, while the covering fraction of the obscuring medium is close to unity, and the equivalent hydrogen column progressively reduces. The flare selected spectra are thereafter much softer, but at the same time, highly photoelectrically absorbed, so that we have extremely poor statistics below 2 keV. The absorbed fluxes in the 1−10 keV range are 5.6×10^{-10}, 7.6×10^{-10}, and 8.5×10^{-10} ergs cm^{-2} s^{-1}, for flares 1, 2, and 3, respectively.

The emission evolution of the continuum is also accompanied by a substantial modification of the spectral features of the source, which is more remarkable in the 6.2−7.4 keV iron region. All the flaring spectra do not present apparent emission lines, but, on the contrary, we observe mostly absorption resonant lines

of H-like and He-like Ca and Fe, together with a broadened Gaussian in the 6.5−6.6 keV energy range.

The H-like resonant iron absorption line is detected in all the flaring spectra, as well as the H-like calcium line (with a significance of ∼4 σ for each spectrum); the widths of both lines are not well constrained by the fit, although the best-fitting values of the Ca XX are consistent with an intrinsic narrowness, while the Fe XXVI line, overall in state 1, is broadened. The He-like calcium absorption line is well detected in two of the three flaring spectra; in flare 1 we had to freeze the value of the line energy to the expected rest-frame value, given that the line appeared rather broadened, while in flare 3 the derived line energy is consistent with the expected value. The He-like Ca line appears, contrary to what found for the corresponding H-like line, intrinsically broadened and more intense.

The He-like iron line is detected only in the last flare, but its position could not reasonably be constrained by the fit and we kept frozen the line energy to the laboratory rest frame. We do not find any evidence of possible Fe Kα line; by fixing the position and the width of the line to the best values of the fit during the quiescent state we derived from the normalization of the line a significance of only ∼1 σ for all the three flaring spectra. We
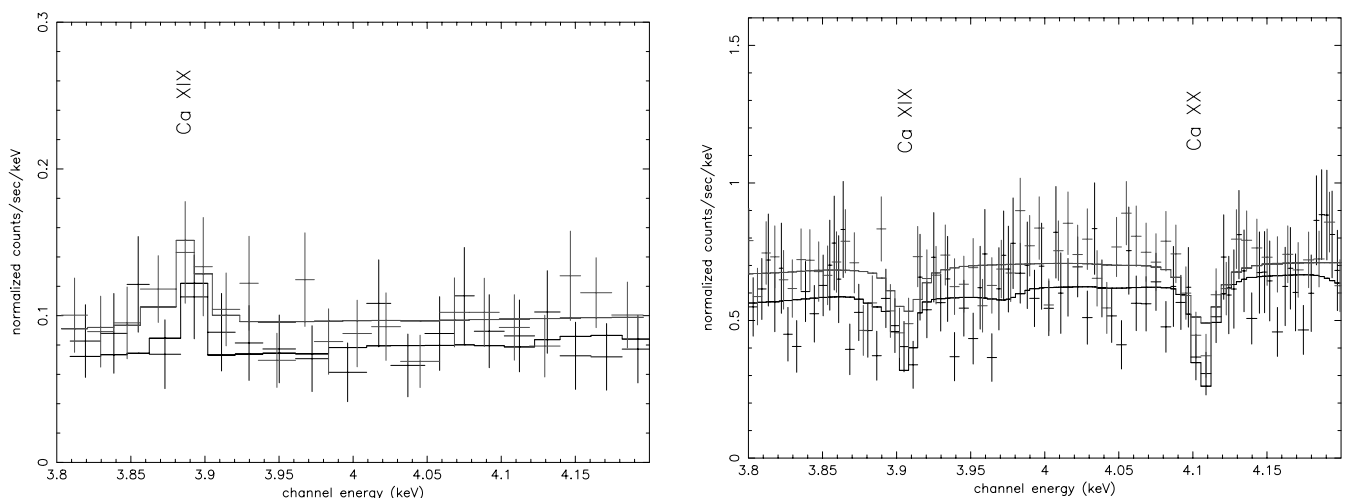

Fig. 4.—Plot of data with best-fit model superimposed for the quiescent/hard state and for the flaring state in the 3.8−4.2 keV Ca region. Best-fitting parameters and associated errors for the continuum emission and of the line emission features are reported in Tables 1 and 2, respectively. MEG data are shown in red, HEG data in black.
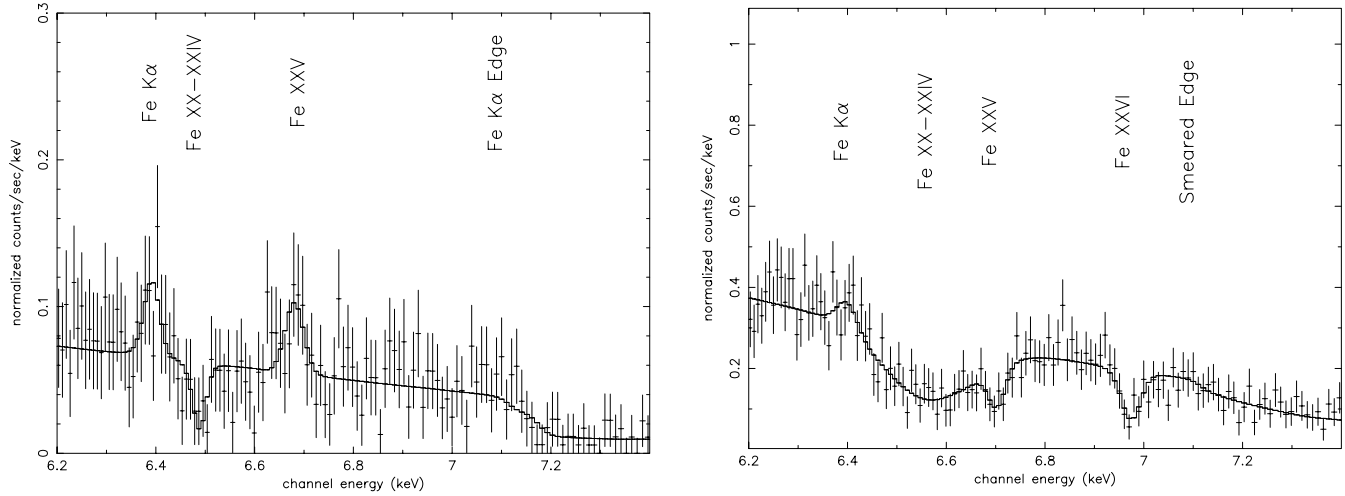
Fig. 5.—Plot of data (no rebin applied) with best-fit model superimposed for the quiescent/hard state and for the flaring state in the 6.2–7.4 keV Fe region. Best-fitting parameters and associated errors for the continuum emission and of the line emission features are reported in Tables 1 and in 2, respectively.

observe in the Fe Kα region, for the first time in this source, a complex broadened feature in absorption at energies between 6.54 and 6.64 keV that can be simply fitted by a broad Gaussian in absorption; we find that this feature is present in each flaring state, and that the energy of the line centroid that does not significantly vary during the three flaring episodes; the width of the line is not always well constrained by the fits, particularly in state 2, where the relative error value is about 50% of the best-fit value; however, for all the states, we find a common range, consistent with all the states, in the 70–100 eV range. Fits with

TABLE 3
THE FLARE STATES

Parameter	Flare 1	Flare 2	Flare 3
kT_{bb} (keV)	$1.60^{+0.09}_{-0.05}$	$1.56^{+0.36}_{-0.11}$	$1.58^{+0.13}_{-0.05}$
L_{bb} (10^{36} ergs s^{-1})	6.44 ± 0.14	8.49 ± 0.36	9.4 ± 0.5
pcfabs N_H (10^{22})	$14.7^{+1}_{-0.7}$	$10.7^{+1.2}_{-1.6}$	$7.0^{+1.4}_{-0.6}$
pcfabs cvr frac	$0.939^{+0.014}_{-0.012}$	0.96 ± 0.03	$0.98^{+0.02}_{-0.01}$
smedge (keV)	$7.14^{+0.18}_{-0.21}$	$7.41^{+0.13}_{-0.3}$	$7.2^{+0.4}_{-0.1}$
smedge τ	$0.60^{+0.16}_{-0.3}$	$0.5^{+0.9}_{-0.3}$	$0.9^{+1.8}_{-0.5}$
smedge (keV)	$0.12^{+0.6}_{-0.09}$	0^{+9}_{-0}	$0.4^{+5}_{-0.4}$
Ca XIX E (keV)	3.902	...	$3.915^{+0.027}_{-0.023}$
Ca XIX σ (eV)	22^{+10}_{-14}	...	30^{+43}_{-11}
Ca XIX flux ($\times 10^{-4}$)	$-3.9^{+2.5}_{-2.6}$	...	-7^{+4}_{-6}
Ca XX E (keV)	4.107	4.107	$4.106^{+0.006}_{-0.006}$
Ca XX σ (eV)	0^{+30}_{-0}	0^{+25}_{-0}	0^{+11}_{-0}
Ca XX Flux	-2.3 ± 1.4	$-4.5^{+2.4}_{-3.4}$	$-3.7^{+1.8}_{-6}$
Fe blended E	$6.58^{+0.02}_{-0.02}$	6.59 ± 0.04	$6.57^{+0.03}_{-0.02}$
Fe blended σ	90^{+17}_{-14}	100^{-30}_{+50}	70 ± 30
Fe blended flux ($\times 10^{-4}$)	-23 ± 4	-31^{+9}_{-12}	-19^{+7}_{-6}
Fe XXV E (keV)	...	...	6.700
Fe XXV σ (eV)	...	...	0^{+23}
Fe XXV flux ($\times 10^{-4}$)	...	...	-5 ± 3
Fe XXVI E (keV)	$6.99^{+0.15}_{-0.04}$	$6.979^{+0.028}_{-0.022}$	$6.972^{+0.08}_{-0.017}$
Fe XXVI σ (eV)	32^{+38}_{-20}	8^{-8}_{+70}	6^{+60}_{-6}
Fe XXVI flux ($\times 10^{-4}$)	-5.4 ± 3	-9^{+5}_{-18}	-4.5^{+3}_{-6}
χ^2/dof	303/496	190/364	279/533

NOTES.—Fitting results for the continuum model and absorption-line features in the Cir X-1 first-order HEG and MEG spectra for the three time-selected spectra during episodes of flaring activity. Line flux is in units of photons cm^2 s^{-1}. Blackbody luminosity is calculated considering a distance to the source of 6 kpc. Uncertainties are reported at 90% confidence level for a single parameter; upper limits at 95% confidence level.

two, or more, Gaussians replacing the single Gaussian did not provide significant changes in the χ^2 value of the fit.

In each flaring state we find that spectrum falls above 7 keV more rapidly than the expected best-fit model. We therefore added an edge component, as also expected to be present from the complex absorption features in the 6.4–7.0 keV energy range. Using the edge component, we find, for each flare state, a threshold energy at $\sim$7.4 keV, with an optical depth that is almost constant during the different flares at $\tau \sim 0.5$. Replacing the edge component with the smeared edge component smedge slightly improves the χ^2 value of the fit, although not significantly, and generally we find only upper values to the smearing width (see Table 3).

Given the presence of the line features, and their general consistency, in the three flaring spectra and the smooth continuum evolution of the source, we decided to merge the three spectra into a single spectrum in order to increase the statistics and to better constrain features present in each flare state. Although there is a significant change in the continuum parameters (mainly in the total luminosity of the source and in the N_H value of the pcfabs component), our main focus is addressed to the detected emission/absorption features, and we use the continuum for the detection of the local emission/absorption lines. We report the best-fit continuum parameters and associated errors in the second column of Table 1, while the parameters of detected features are summarized in Table 2. The merged "flare" spectrum shows emission features that were statistically hidden by the short exposure times. However, we choose to fix line energy or/and line width to the value of the total time integrated spectrum (see next section), in order to derive a better constraint to the line fluxes, in cases where the fit could not constrain all the line parameters at the same time. In particular, the spectrum shows the resonant emission line of Si XIV and S XVI (see Fig. 3, *right panel*) and the Fe Kα emission line at 6.4 keV. It is to be noted, however, that the flux of the Si XIV line results much higher with respect to the corresponding value during the hard state. We do not find any evidence of the presence of the Ca XIX emission line, but we observe the corresponding absorption line, together with the Ca XX absorption line (see Fig. 4, *right panel*). The iron region is dominated by three broad absorption lines: the blended Fe XX–Fe XXIV line at 6.57 keV line, the He-like Fe absorption line at 6.70 keV, and the H-like line at 6.97 keV. A plot of the data with superimposed best-fit model for this energy region is shown in the right panel of Figure 5.
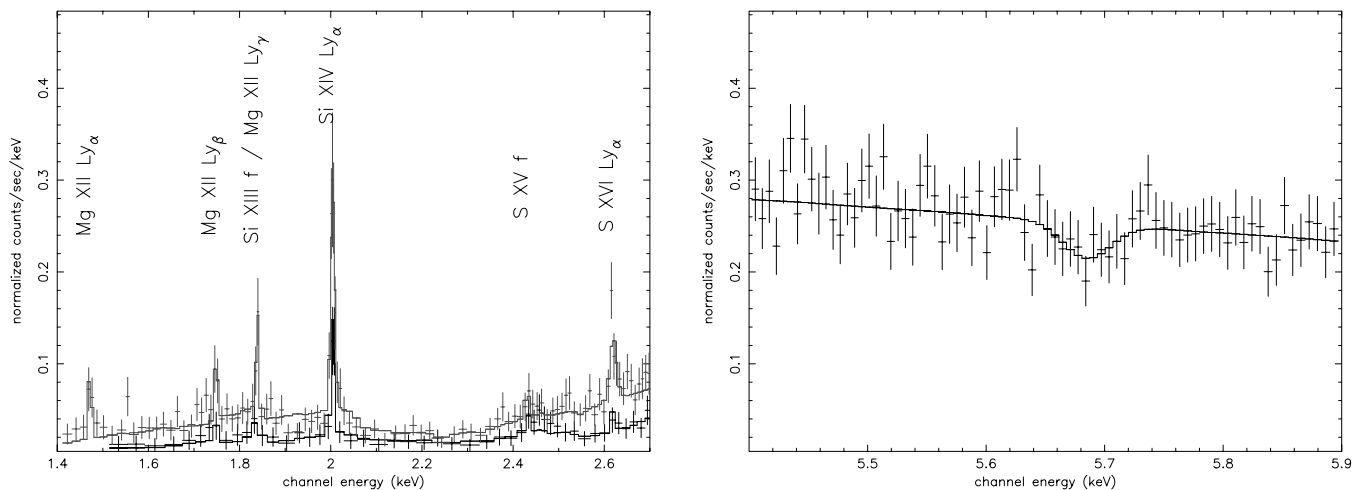
FIG. 6.—*Left:* Data together with best-fit model in the low-energy band (1.4−2.7 keV) for the total time integrated spectrum. *Right:* An identified absorption feature in the same spectrum at 5.689 keV. See discussion.

3.3. *The Total Integrated Spectrum*

As a final step in our analysis we produced a time-integrated first-order HEG/MEG spectrum of the entire observation, as it will prove helpful for detecting features that are statistically damped by the low S/N of short time exposure spectra. The continuum spectrum is obviously to be taken as rather indicative of the merging of the hard quiescent state and of the softer, but much more absorbed, flaring state. The best-fitting values of the continuum, in fact, reflect a weighted average of the changing spectrum of the source, and, as in the case of the merged flare spectrum, this will mainly serve to put a continuum under the detected features. For completeness' sake, however, we report these values in the last column of Table 1.

On the soft part of the spectrum the emission lines belonging to H-like ions of Mg XII (Lyα, Lyβ, and Lyγ), Si XIV (Lyα), and S XVI (Lyα) are clearly detected. However, the high flux and equivalent width of the Mg XII Lyγ, which are both comparable to the value of the Mg XII Lyβ, are indicative of a possible blending with the forbidden line of Si XIII, whose rest-frame energy position is at 1.8397 keV. We, then, looked for the corresponding He-like resonance lines for these elements by locally adding Gaussian emission lines, fixing the line energies at 1.3522, 1.8449, and 2.4606 keV for Mg XI, Si XIII, and S XV, respectively, and leaving width and normalization of each line as free parameters. The significance of these lines resulted always less than 2 σ. Given the highly probable presence of the forbidden line of Si XIII, we looked for the other forbidden lines of S XV, Ca XIX, and Fe XXV. Fixing the centroid line energies to the expected rest-frame values (2.4307, 3.8612, and 6.6366 keV), and the widths of the lines at 2 eV (fit was not sensitive to variations of this parameter), we obtained a significance of 2.6, 2.8, and less than 1 σ for S XV, Ca XIX, and Fe XXV, while the best-fit equivalent widths were, respectively, 10, 3, and 4 eV. Although the significance of the forbidden line of Fe XXV is very low, we note that the spectrum is strongly curved by a broad absorption feature at ∼6.5 keV that, together with the merged changing continuum, can have a strong smearing effect on this emission line. A closer inspection of these features, using unbinned spectra, revealed that the centroid energy lines well match the peak of the Gaussian profiles, with an uncertainty of just few eV.

The Si XIV and S XVI lines present a small redshift with respect to the expected rest-frame values, while the other emission lines present values consistent with rest-frame measurements. We note

that the detected forbidden lines are hard to be interpreted as redshifted resonance lines, given that the energy separation between the forbidden and the resonance is in the range 25−40 eV for the He-like ions under consideration, while the redshift as measured from the H-like emission line is a few eV. We cannot, however, exclude that the intercombination lines can be partially blended with the forbidden ones.

The widths of the lines (except for the Mg XII Lyα and Lyβ, which were unconstrained by the fit, so that we choose to fix the values of these parameters to a reference value of 2 eV) are generally broadened by a few electronvolts. We show data, with superimposed best-fit model, in this soft X-ray region (1.4−2.7 keV) in the left panel of Figure 6. The Ca XIX resonant emission line, present during the quiescent state, is no longer detected in the total average spectrum, probably due to the stronger continuum flux at this energy, or, more probably, by the combined effect of emission (during the hard state) and absorption (during the flaring state) seen in the time-selected spectra, but we consider highly significant the detection of the forbidden line of Ca XIX. We also observe in the spectrum an absorption line at 5.689 ± 0.016 keV, σ = 0.013 (upper value 0.03) and equivalent width of 7 eV, that is hard to identify with a resonance line of any element. Its significance is at ∼3 σ. This feature was not detected in the quiescent/hard spectra, while in the flare integrated spectrum this feature is required at 2.8 σ. In the 6.4−7.1 keV energy band the spectrum closely follows the shape of the spectrum during the flaring episodes, showing the iron Fe Kα emission line, a broad absorption feature in the 6.5−6.6 keV range and the Fe XXV and Fe XXVI resonant absorption lines. We also check for two expected further absorption edges at fixed energy position, corresponding to the expected edges of Fe XXV (8.828 keV) and Fe XXVI (9.278 keV), obtaining for the corresponding optical depth the best-fit values of 0.2 and 0.6 (upper values of 0.6 and 1.3 for the He-like and H-like ion, respectively). We present at the end of Table 2 the identified emission and absorption features in this case. After having verified that every part of the spectrum was free from any other significant residual, we obtained a final χ^2 value of 1004 for 1384 degrees of freedom.

4. DISCUSSION

In the *Chandra* observations performed in 2000 (Schulz & Brandt 2002), the Cir X-1 spectrum clearly showed a rich variety of emission/absorption features, the most striking of which were

resolved P Cygni profiles of He- and H-like elements. This observation is taken at a higher orbital phase with respect to the almost phase-zero observations I and II in Paper I. Compared to the previous observations, we observe in this case two different spectral states, within the same observational window. A low-count-rate quiescent state, followed by more complex, highly variable, flaring states. We do not detect any P Cygni profile in the spectrum, but we observe resonant emission lines from H-like ions of Mg, Si and S, the forbidden lines of He-like Si, S, and Ca, the Fe Kα fluorescence line at $\sim$6.4 keV, and a complex variable absorption pattern in the Fe Kα region during the flaring states of the source.

4.1. *The Continuum Emission*

During the quiescent state the source should be accreting at a few percent of its Eddington limit (for an assumed distance of 6 kpc and for a 1.4 $M_{\odot}$ NS), which is considerably less than what reported for observation I ($\sim$at the Eddington limit) and observation II ($\sim$10% L_{Edd}) in Paper I. Although the limited energy coverage and the low counting statistics of *Chandra* can give only a first-order approximation to the real broadband spectrum, we note that the continuum spectrum is not similar to any previously observed spectrum of this source. Its rather hard shape is much closer to that of a typical accretion powered pulsar (Zurita Heras et al. 2006); also, the derived blackbody temperature is too high to be taken as a thermalized blackbody temperature of the inner accreting regions. The primary X-ray source results partially absorbed by a cold neutral medium that, however, does not completely screen out the primary X-ray flux. The derived column density of the absorbing material is not compatible with the (2.3 $\pm$ 0.2) $\times 10^{22}$ cm^{-2} of the zero-phase observations; we note about 1 order of magnitude increase during our observation, with also an increased value of the covering fraction. The spectrum in this state also shows a strong Fe Kα edge, and, although the value of the derived optical depth cannot be well constrained by the fit, as this is entangled with the derived column density of the partial covering component, its increase, with respect to the phase-zero observations, seems to correlate with the increase of the column density of the partial covering medium, thus leading to the conjecture that iron present in the neutral medium is strongly overabundant with respect to the interstellar abundance.

The lack of P Cygni profiles in the spectrum during this observation could be related to the change in luminosity of the primary X-ray flux: the reduced irradiating flux with respect to the past *Chandra* observations might not be able to consistently evaporate part of the accretion disk, or, alternatively, the disk may not be present and matter may accrete onto the compact object along a direction that we do not directly observe (the absence of any softer component in the spectrum could also indicate that the accretion disk does not contribute to the X-ray luminosity and that it may be truncated at a large distance from the compact object).

The spectral continuum shape has a dramatic change during the flaring state. Previous models considered that the dipping activity in Cir X-1 could be related to the almost edge-on geometry of the system that makes our line of sight directly plunge into the turbulent accreting external layers of an accretion disk (Shirey et al. 1999). This scenario explains the light-curve variability as a combined effect of the variable accretion rate and of the change in density of the colder accreting material. In this observation the major difference in the preflaring and the flaring states is the fraction of the partial covering component of the primary X-ray flux, together with an increased continuum luminosity. If this is a consequence of a turbulent higher mass accretion rate, it can

be argued that this is also the cause of a geometrical inflation of the occulting medium giving the increase in the covering fraction.

During the flaring states, the soft emission lines are more difficult to detect, given the high photoelectric absorption at these energies. However, the total "flare" spectrum show that these features continue to be present in the spectrum, growing in intensity with respect to the quiescent/hard state, in correlation with a more intense irradiating continuum flux.

Boirin et al. (2005), analyzing the spectrum of the source 4U 1323$-$63 in a dipping and in a persistent state, found that spectral changing could be modeled by variations in the properties of a neutral and of an ionized absorber. We suggest that Cir X-1 could also represent a paradigmatic example of the complex interplay of these two absorbers. Moreover, in Cir X-1 there could also be a rapid changing in the geometry of the emitting media; a proof of that may be given by the emission line of Fe XXV that we observe during the quiescent state and that appears in absorption during the flaring state.

4.2. *Line Diagnostics: Indications of a Hot, Photoionized, Plasma*

The features that we observe in emission during the quiescent state are from H-like Si, and from He-like Ca and Fe; we argue that the low-energy detected emission lines in the total integrated spectrum of Mg XII (where we detect the Lyα, Lyβ, and Lyγ transitions), S XVI, and the forbidden He-like lines of Si XIII (blended, however, with the Mg XII Lyγ), S XV, and Ca XIX, could also be common features in the quiescent/hard spectrum, not revealed only because of the low statistics. Under this assumption, we infer that the weakness of the He-like emission lines translate into a rather higher value of the ionization parameter with respect to the value reported in Paper I. The ionization parameter $\xi = L/n_e r^2$ (where n_e is the electron density, r is the distance from the source, and L is the X-ray luminosity) that characterizes the Mg, Si, and S H-like ions and avoids having appreciable fractions of the corresponding He-like ions, is above log $\xi > 3$, in the limit of a low-density gas and a hard ionizing flux, $F_{\mathrm{ion}} \propto E^{-1}$ (Kallman & Bautista 2001).

We consider the detection of the forbidden lines of Si XIII, S XV, and Ca XIX as a strong confirmation of the photoionized nature of the emitting plasma. However, we note that the relative weakness/absence of the resonance lines could also be ascribed to the fact that line-resonance photons can be trapped inside the emitting plasma, being multiply emitted and reabsorbed. If the thermal electron temperature is in the 10^6–10^7 K range, then Compton scattering of the line photons will lead to a strong line broadening, thus making them hard to detect. Forbidden lines photons will, on the contrary, easily escape the emitting medium, thus preserving line narrowness.

These lines appear, at least the ones that are statistically better constrained, broadened, the broadening being stronger for lower Z elements. Their relative widths [$\Delta E/E \sim (1.5$–$3) \times 10^{-3}$] can be due to a combination of thermal, rotational, and turbulent effects. We also note a slight redshift of the brightest lines; we also verified the common redshift of the emission lines, and their common origin, by leaving as a free parameter only the Si XIV centroid energy and fixing the other line energies at the expected rest-frame difference (i.e., $E_{\mathrm{S\ XVI}} = E_{\mathrm{Si\ XIV}} + 0.6162$ keV, and similarly for the other H-like emitting lines), in the total time integrated spectrum. We found that the fit is equivalent to one for which the line energies are free parameters, and all the emitted lines, if Doppler-redshifted, share a common radial velocity of about $\sim$40 km s^{-1}.

The significance of this result is at more than 2 σ confidence level. Schulz & Brandt (2002) derived from the He-like resonance forbidden and intercombination lines of the He-like Mg XII a value $G = F_i + F_z/F_r = 2.9 \pm 1.0$, where F_i, F_z, and F_r are, respectively, the flux values of the intercombination, forbidden, and resonance lines, which strongly indicates the presence of a photoionized plasma (Porquet & Dubau 2000) as the proper line-emitting region. During this *Chandra* observation, we do not observe the He-like resonance lines, while the intercombination lines cannot be clearly resolved, so that we cannot appropriately use the R and G diagnostics to infer the physical properties of the emitting plasma. However, as pointed out by Porquet & Dubau (2000) the presence of forbidden lines and the weakness of the resonant ones is by itself a good indication of the photoionized nature of the emitting plasma.

Using the calculations present in Porquet & Dubau (2000), we derive from the intensity of the forbidden line of Si XIII an upper limit to the plasma density of n_e of 10^{13} cm^{-3}. The intensity of the H-like lines, compared to the corresponding He-like lines, gives a second important clue, namely, that the plasma temperature is extremely high (in the range 10^6–10^7 K) in order to allow a high ratio of the H-like ion population to the He-like one. The plasma is, therefore, dominated by recombination, rather than by collisional excitation.

4.3. *Absence of Radiative Recombination Continua*

Another characteristic signature of a purely photoionized plasma would be the detection of the radiative recombination continuum (RCC), which should appear in the spectrum as an emitting line feature just above the K H-like/He-like ion edge. We do not observe any RCC feature above the K edge of Mg XII, Si XIV, and S XVI, both in the quiescent/hard region and in the flaring state. If the emitting plasma is strongly photoionized, we note that the lack of such features could generally be ascribed to one or more of the following physical processes (Bautista et al. 1998): three-body recombination, collisional excitation, or resonant fluorescent excitation. The first mechanism will operate in a regime of very high density and low temperature; however, for very high Z elements, such as Si and S, this process is not competitive with radiative recombination (as three-body recombination coefficient scales very rapidly with nuclear charge Z, as Z^{-6}), and its impact is to be considered marginal. Collisional excitation, on the other hand, is a viable candidate process for populating $n = 2$ levels, opposed to radiative recombination, provided that temperatures are in excess of 10^6 K and there is a significant fraction of H-like ions in the ground state, but the presence of forbidden lines indicate that plasma density is extremely low to allow collisions to efficiently operate. Finally, photoexcitation is a very efficient way to populate upper levels, but it imposes a particular geometry of the X-ray-emitting continuum region and line emitting region, i.e., that the emitting photoexcited plasma is located away from the source of the X-ray continuum and is not located between the X-ray source and the observer. Another, perhaps simpler, explanation is that RCC is undetected because the plasma is hot enough to smear out RCC photons into the continuum (the broadening of this feature depends on temperature and is stronger for higher temperatures; see Liedahl & Paerels 1996).

4.4. *The Iron and Calcium Features*

The presence of the fluorescence line of the Fe Kα during the quiescent emission could be due, as in the case of the H-like emission lines at lower energies, to reflection in the colder border of the accretion disk of the primary X-ray incident flux. The line

could be broadened by the blending of all the low-ionization states of iron (Fe I–Fe IX), and we also observe that the corresponding edge has an edge energy that is slightly higher than the rest-frame expected threshold at 7.11 keV, thus supporting the idea that a consistent fraction of the reflecting iron is in a low-ionization state (Kallman & Bautista 2001). This state shows only one clearly detected absorption feature at $\sim$6.49 keV. We take as highly improbable the origin of this feature as a blueshifted Fe Kα line of nearly neutral photoionized iron, given the required extreme high bulk velocity of the absorbing medium (3700^{+1800}_{-800} km s^{-1}). On the contrary, we are led to interpret this feature, according to the calculations of Kallman et al. (2004) as blending of absorption resonant transitions of Fe XX–Fe XXIV. This is the first observation where resonant blended absorption features of intermediate ionization states of iron are observed in the spectrum of Cir X−1.

As in the cases of 4U 1323−62 (Boirin et al. 2005), MXB 1659−298 (Sidoli et al. 2001), X1624−49 (Parmar et al. 2002), and GX 13+1 (Sidoli et al. 2002), we also find a broad line centered at energies between 6.5 and 6.6 keV; however, the Cir X-1 spectrum shows this feature in absorption, while in the other sources it was observed in emission. We also note that the large width associated with this feature could also indicate a rather large gradient in the velocity field of the absorbing medium; the Fe XXV and Fe XXVI lines, which are both better resolved in the total integrated spectrum, are strongly broadened and are blueshifted with respect to the rest-frame energies. Together with the absorption feature of Ca XX, these lines give an average blueshift of 370 ± 100 km s^{-1} that we interpret as due to a bulk motion of the absorbing medium. We also note that this value is significantly lower with respect to the reported past *Chandra* observations in Paper I, where the H-like and He-like iron lines showed a $\sim$1000 km s^{-1} blueshift.

If we neglect the filling effect of the emission lines observed during the quiescent state, and if we make the assumption that the lines are not saturated, we can derive a rough estimate (to be more rightly intended as lower limits) of the column densities of the absorbing hot cloud from the absorption lines of H-like and He-like iron, using the calculations of Spitzer (1978) with the relation

$$\frac{W_\lambda}{\lambda} = \frac{\pi e^2}{m_e c^2} N_j \lambda f_{ij} = 8.85 \times 10^{-13} N_j \lambda f_{ij},$$

where N_j is the column density for the relevant species, f_{ij} is the oscillator strength and W_λ the equivalent width of the line and λ is the wavelength expressed in cm.

Adopting $f_{ij} = 0.798$ and $f_{ij} = 0.416$ for Fe XXV and Fe XXVI, respectively (Verner & Yakovlev 1995), and the best-fitting parameters of Table 2, we derived from the best-fitting parameters a column density of $\sim$2.3 $\times 10^{17}$ and 8.3×10^{17} cm^{-2} for Fe XXV and Fe XXVI, respectively. This rough estimation allows us to derive the ratio of the ionization fractions of the two ion species ($\sim$3.6), and to assign a logξ value for the ionization parameter $\sim$4.2 (Kallman & Bautista 2001).

The ratio of the H-like/He-like abundances of calcium suffer for larger uncertainties, but still the value of the ionization parameter that we derived (log $\xi \sim 3.5$ from the best-fitting values) confirms the presence of an extremely photoionized plasma. However, we note that to obtain the observed equivalent width ratio Ca XX/Fe XXVI (neglecting any possible saturation effect on the lines), we infer that calcium must be overabundant by almost an order of magnitude with respect to the cosmic abundances.

The absorption edge that is detected above 7.0 keV, at an energy that is considerably lower than the 7.11 keV expected value, for the Fe Kα edge, could result from the radiative and Auger damping effects after the creation of the K hole (see also Palmeri et al. 2002; Ross et al. 1996). As predicted by the high ionization parameter, the resonances are spread over more than 500 eV width, although we have also to take into account that the strong neutral Fe edge observed during the hard state certainly introduces a significant fraction of fictitious "smearing" in the detected edge.

4.5. *A Highly Redshifted Absorption Line?*

The detection at 3.1 σ significance of an absorption line at 5.689 keV could be due to an extremely redshifted ($z \simeq 0.18$) Fe XXVI line, produced in the photosphere of the compact object. We derive, for a 1.4 $M_\odot$ NS a distance from the compact object of ~ 14 km, if the line is purely gravitationally redshifted, excluding any possible Doppler effect. The absence of substructures in this line, if the line is rotationally broadened, would imply a rotational frequency ≥ 50 Hz (Chang et al. 2006). We note that the presence of this feature, with a slight shift in energy, has also been reported in Iaria (2007) and a similar feature has been also been observed by Longinotti et al. (2007) in the spectrum of the AGN Mrk 335. In the latter case the redshift was interpreted as due to an optical thick radial inflow of the accreting matter near the compact object at $\sim 0.11 - 0.15\,c$ velocity. Such explanation could also apply to the case of Cir X-1, and we computed in this case, neglecting the effects of the radiation pressure on the infalling matter, a distance to the central object of $\sim 60 R_g$. However, further observations are required to confirm this detection.

4.6. *System Geometry*

In the following we explore and discuss two possible geometrical scenarios for the system.

The presence of highly ionized absorption features during flaring episodes, together with emission features from H-like ions, requires two spatially distinct zones; one optically thick region, with a large ξ gradient, rapidly varying according to the global luminosity/accretion rate of the source, owing also large gradient velocity fields; and a second zone, optically thinner, photoionized plasma that is present during both the persistent emission and the flaring episodes. Jimenez-Garate et al. (2002) calculated the effects of a hard X-ray source illuminating an accretion disk; it is shown that above an assumed Shakura-Sunyaev disk (Shakura & Syunyaev 1973) and under hydrostatic balance, there is a natural split into a two-zone medium: a warm corona, or atmosphere, where photoionization and radiative recombination balance energetically each other, and a hot corona, dominated by the balance of Compton heating and cooling. The total volume, ionization fraction, and density in the two zones determine the strength of the emission/absorption features impressed in the total spectrum. The weakness of He-like ions lines during our *Chandra* observation (with the only exception of the He-like Ca XIX emission line in the hard state), compared to previous *Chandra* observations, could be traced back in the interplay of these two zones. If the He-like emitting region is the colder atmosphere and the H-like emitting region is set inside the hot corona, then the ratio of the H-like/He like emission lines indicates a different ratio of the emitting volumes, given also that the ionization structure above the photosphere does not sensibly depend on the primary X-ray luminosity. If a thermal instability is operating, then our observation can be in agreement with a condensing solution for the disk atmosphere. Such scenario has, however, two open problems: where to locate the optically thicker absorbing medium during the flare episodes and how to account for the redshift of the emitting lines and the blueshift of the absorption ones. As also pointed out by Jimenez-Garate et al. (2002), the presence of strong outflows/inflows in an accreting system breaks up the assumption of local hydrostatic balance, and the solutions for the disk atmosphere can offer only a partial, or maybe incorrect, modeling. We can only argue that the absorbing plasma, for the required high ionization parameter and density, can be located in the inner part of the accretion flow, where a strong magnetic field prevents the flow from entering the inner part of the system where it would disrupt the accretion disk. Part of this hot, optically thick matter can eventually be expelled from the system, during periods of turbulent enhanced accretion, at this radius, causing the observed blueshift. On the other hand, if the emitted lines are produced inside a disk corona, the redshift is caused again by Doppler motion of the emitting plasma, dragged toward the accretor.

Alternatively, we point out a second viable scenario that has recently emerged (Iaria 2007). Emission features occur in a beamed outflow, which could be seen as the X-ray counterpart of the radio jet observed by Fender et al. (2004). The intensity of the redshift of the lines depends on the inclination of the outflow with respect to our line of sight. Absorption features are located, on the other hand, in an optically thick wind-driven corona; the spectrum is signed by the sampling of the primary continuum into regions characterized by a gradient of the ionization parameter, optical depth, and outflow velocity field. The passage from the quiescent state to the flaring activity causes an a geometrical inflation of the wind that at the outer radius completely screens the central X-ray-emitting object, while in the inner regions gives the resonant features of highly ionized elements. Given the geometrical constraints of the get geometry (Fender et al. 2004; Tudose et al. 2006), this scenario, however, requires that the system geometry is not perfectly edge-on and contradicts the theoretical expectation of an optically thin plasma above the disk.

4.7. *Conclusions*

We analyzed *Chandra* HETGS data of Cir X-1 during phase passage $0.223 - 0.261$. Based on the flux variability, the source clearly showed a complex spectral changing both in the continuum and in the features. This observation reveals the following, partly new, aspects of this source:

1. The passage from a quiescent to a flaring activity determines a change both in the luminosity and in the covering fraction of the absorbing medium that during the flare almost completely screens out the source of the continuum emission.

2. During flare episodes the 6.4–7.0 keV region is dominated by broad absorption lines of moderately and highly ionized iron ions that cover a large range of possible ionization factors.

3. During flaring the source still displays emission lines, whose intensity increases with increased continuum luminosity.

4. Emission lines stem from a purely photoionized medium with temperatures in excess of 10^6 K and electron density below $n_e \sim 10^{13}$ cm^{-3}.

5. We found a possible detection of a strong redshifted Fe XXVI absorption line at $z = 0.18$.

REFERENCES

Bautista, M. A., Kallman, T. R., Angelini, L., Liedahl, D. A., & Smits, D. P. 1998, ApJ, 509, 848
Belloni, T., Méndez, M., & Homan, J. 2007, MNRAS, 376, 1133
Boirin, L., Méndez, M., Díaz Trigo, M., Parmar, A. N., & Kaastra, J. S. 2005, A&A, 436, 195
Boutloukos, S., van der Klis, M., Altamirano, D., Klein-Wolt, M., Wijnands, R., Jonker, P. G., & Fender, R. P. 2006, ApJ, 653, 1435
Brandt, W. N., Fabian, A. C., Dotani, T., Nagase, F., Inoue, H., Kotani, T., & Segawa, Y. 1996, MNRAS, 283, 1071
Chang, P., Morsink, S., Bildsten, L., & Wasserman, I. 2006, ApJ, 636, L117
Clark, D. H., Parkinson, J. H., & Caswell, J. L. 1975, Nature, 254, 674
Clark, J. S., Charles, P. A., Clarkson, W. I., & Coe, M. J. 2003, A&A, 400, 655
Clarkson, W. I., Charles, P. A., & Onyett, N. 2004, MNRAS, 348, 458
Ebisawa, K. 1991, Ph.D. thesis (Univ. Tokyo; ISAS Research Note 483)
Fender, R., Spencer, R., Tzioumis, T., Wu, K., van der Klis, M., van Paradijs, J., & Johnston, H. 1998, ApJ, 506, L121
Fender, R., Wu, K., Johnston, H., Tzioumis, T., Jonker, P., Spencer, R., & van der Klis, M. 2004, Nature, 427, 222
Glass, I. S. 1994, MNRAS, 268, 742
Haynes, R. F., Jauncey, D. L., Murdin, P. G., Goss, W. M., Longmore, A. J., Simons, L. W. J., Milne, D. K., & Skellern, D. J. 1978, MNRAS, 185, 661
Haynes, R. F., Komesaroff, M. M., Jauncey, D. L., Caswell, J. L., Milne, D. K., Kesteven, M. J., Wellington, K. J., & Preston, R. A. 1986, Nature, 324, 233
Heinz, S., Schulz, N. S., Brandt, W. N., & Galloway, D. K. 2007, ApJ, 663, L93
Iaria, R., Burderi, L., Di Salvo, T., La Barbera, A., & Robba, N. R. 2001a, ApJ, 547, 412
Iaria, R., Di Salvo, T., Burderi, L., & Robba, N. R. 2001b, ApJ, 561, 321
Iaria, R., et al. 2007, ApJ, submitted
Jimenez-Garate, M. A., Raymond, J. C., & Liedahl, D. A. 2002, ApJ, 581, 1297
Jonker, P. G., Nelemans, G., & Bassa, C. G. 2007, MNRAS, 374, 999
Kallman, T., & Bautista, M. 2001, ApJS, 133, 221
Kallman, T. R., Palmeri, P., Bautista, M. A., Mendoza, C., & Krolik, J. H. 2004, ApJS, 155, 675
Kaluzienski, L. J., Holt, S. S., Boldt, E. A., & Serlemitsos, P. J. 1976, ApJ, 208, L71

Liedahl, D. A., & Paerels, F. 1996, ApJ, 468, L33
Longinotti, A. L., Sim, S. A., Nandra, K., & Cappi, M. 2007, MNRAS, 374, 237
Mignani, R. P., De Luca, A., Caraveo, P. A., & Mirabel, I. F. 2002, A&A, 386, 487
Morrison, R., & McCammon, D. 1983, ApJ, 270, 119
Palmeri, P., Mendoza, C., Kallman, T. R., & Bautista, M. A. 2002, ApJ, 577, L119
Parkinson, P. M. S., et al. 2003, ApJ, 595, 333
Parmar, A. N., Oosterbroek, T., Boirin, L., & Lumb, D. 2002, A&A, 386, 910
Porquet, D., & Dubau, J. 2000, A&AS, 143, 495
Ross, R. R., Fabian, A. C., & Brandt, W. N. 1996, MNRAS, 278, 1082
Schulz, N. S., & Brandt, W. N. 2002, ApJ, 572, 971 (Paper I)
Schulz, N. S., Kallman, T. E., Galloway, D. K., & Brandt, W. N. 2007, preprint (arXiv: 0709.3336)
Shakura, N. I., & Syunyaev, R. A. 1973, A&A, 24, 337
Shirey, R. E., Levine, A. M., & Bradt, H. V. 1999, ApJ, 524, 1048
Sidoli, L., Oosterbroek, T., Parmar, A. N., Lumb, D., & Erd, C. 2001, A&A, 379, 540
Sidoli, L., Parmar, A. N., Oosterbroek, T., & Lumb, D. 2002, A&A, 385, 940
Spitzer, L. 1978, Physical Processes in the Interstellar Medium (New York Wiley)
Stewart, R. T., Caswell, J. L., Haynes, R. F., & Nelson, G. J. 1993, MNRAS, 261, 593
Stewart, R. T., Nelson, G. J., Penninx, W., Kitamoto, S., Miyamoto, S., & Nicolson, G. D. 1991, MNRAS, 253, 212
Tauris, T. M., Fender, R. P., van den Heuvel, E. P. J., Johnston, H. M., & Wu, K. 1999, MNRAS, 310, 1165
Tennant, A. F., Fabian, A. C., & Shafer, R. A. 1986, MNRAS, 221, 27P
Tudose, V., Fender, R. P., Kaiser, C. R., Tzioumis, A. K., van der Klis, M., & Spencer, R. E. 2006, MNRAS, 372, 417
Verner, D. A., Ferland, G. J., Korista, K. T., & Yakovlev, D. G. 1996, ApJ, 465, 487
Verner, D. A., & Yakovlev, D. G. 1995, A&AS, 109, 125
Zurita Heras, J. A., de Cesare, G., Walter, R., Bodaghee, A., Bélanger, G., Courvoisier, T. J.-L., Shaw, S. E., & Stephen, J. B. 2006, A&A, 448, 261

Note added in proof.— After acceptance of our paper, we became aware that other authors (Schulz et al. 2007) presented, independently from us, their results based on a spectral analysis of the same data set analyzed here.